

See discussions, stats, and author profiles for this publication at:  
<https://www.researchgate.net/publication/229116835>

# Raman Spectra and Vibrational Analysis of Nanometric Tetragonal Zirconia Under High Pressure

ARTICLE *in* JOURNAL OF PHYSICS AND CHEMISTRY OF SOLIDS · APRIL 2000

Impact Factor: 1.85 · DOI: 10.1016/S0022-3697(99)00242-5

---

CITATIONS

86

---

READS

87

2 AUTHORS, INCLUDING:



Pierre Bouvier

Institut Néel

126 PUBLICATIONS 2,546 CITATIONS

SEE PROFILE

# Raman spectra and vibrational analysis of nanometric tetragonal zirconia under high pressure

P. Bouvier\*, G. Lucazeau

*Laboratoire d' Electrochimie et de Physicochimie des Matériaux et des Interfaces, (LEPMI-UMR 5631 INPG-CNRS), 1130 Rue de la piscine, BP75, Domaine Universitaire, 38402 St Martin d' Hères Cedex, France*

Received 9 October 1998; accepted 22 June 1999

## Abstract

Raman spectra of nanometric tetragonal zirconia have been recorded under high pressure up to 31 GPa. The two lowest frequency modes exhibit an unusual over-damped soft mode behaviour upon increasing pressure. The non-crossover of these modes is the indication that they belong to the same symmetry and this lead us to reconsider the previous normal mode assignment. A new assignment of Raman active mode is deduced from normal mode calculations based on the linear chain model. The continuous loss of intensity and the softening of the  $E_g$  low frequency mode are likely associated with a phase transition which could take place around 38 GPa. The discussion of an evolution of the compound towards a possibly distorted fluorite-like structure at high pressure is based on the reduction of the number of Raman bands and on the decrease of the anisotropy of the microscopic compressibility coefficients estimated from the pressure evolution of force constants. © 2000 Elsevier Science Ltd. All rights reserved.

**Keywords:** A. Nanostructures; C. High-pressure; C. Raman spectroscopy

## 1. Introduction

Zirconia ( $ZrO_2$ ) undergoes polymorphic transformations with change in external parameters. At high temperature, the compound is highly defective and its structure is fluorite type ( $O_h^5$ ). The decreasing temperature induces a cubic to tetragonal ( $D_{4h}^{15}$ ) phase transition ( $c-t$ ) at around 2300°C [1]. This transition is followed by a tetragonal to monoclinic ( $C_{2h}^2$ ) well-known martensitic phase transition ( $t-m$ ) with further cooling. With increasing external pressure the monoclinic phase transforms into an orthorhombic phase at 3 GPa [2]. At 20 GPa and high temperature (1000°C), it transforms into another orthorhombic structure [2–4]. The first transition pressure is particularly sensitive to the sample history [3]. Furthermore, recent Raman characterisation performed on zirconia films grown during the oxidation of Zircaloy-4 alloys seems to demonstrate that tetragonal zirconia can also be stabilised by pressure [5].

$ZrO_2$  structure also depends upon the presence of dopants ( $MgO, CaO, Y_2O_3$ ) which induces disorder in oxygen

position [6]. An addition of 3 wt%  $Y_2O_3$  stabilises the tetragonal form ( $t'$ ) at room temperature [7]. The contribution of the surface energy also influences the structural stability of nanocrystallites. A crystallite size of 30 nm or lower is now believed to stabilize the tetragonal form at room temperature [8]. This critical size seems to depend upon the dopant rate. Recent research on the understanding of the mechanisms involved in the cubic–tetragonal–monoclinic structural transitions suggested that they result from two successive condensations of Brillouin Zone (BZ) boundary phonons [9,10]. One component of the  $X_2^-$  triply degenerate phonon in the cubic phase transforms into a zone centre  $A_{1g}$  phonon in the tetragonal form. A calculation based on a quasi-harmonic lattice-dynamical model confirms the exclusively soft-mode mechanism of the lattice transformation of zirconia [11,12]. However, the presence of a totally symmetric soft mode in the Raman spectra of tetragonal phase has not been confirmed. Finally, the symmetry attribution given by Feinberg et al. [13] are in contradiction with the calculations of Mirgorodsky et al. [12].

The aim of this investigation was to follow the effect of hydrostatic compressive stresses on the structure of undoped

\* Corresponding author.

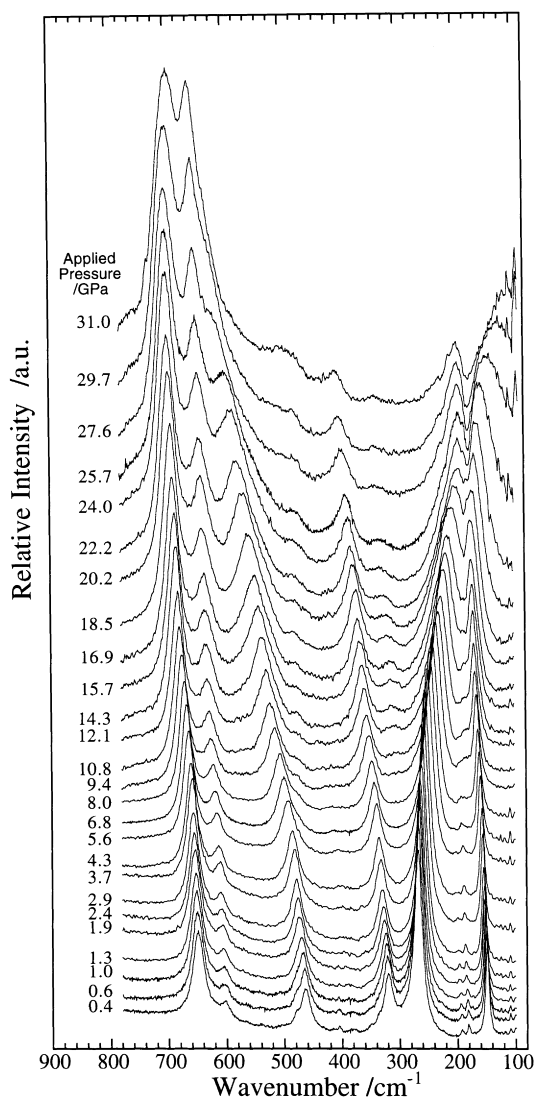


Fig. 1. Raman spectra versus increasing hydrostatic pressure from atmospheric to 31 GPa. The applied pressure is reported on the left side of each spectra.

tetragonal zirconia and to compare the negative volume variations ( $\Delta V_T$ ) and ( $\Delta V_P$ ) induced by the pressure increase and the temperature decrease, respectively. After reporting the experimental result we present the frame in which the linear chain model is used. A new assignment is proposed and an estimate of the microscopic compressibility coefficients is calculated from pressure evolution of force constants.

## 2. Experimental procedure

Chemically pure Tetragonal Polycrystalline Zirconia (TPZ) powder was obtained at low temperature by a

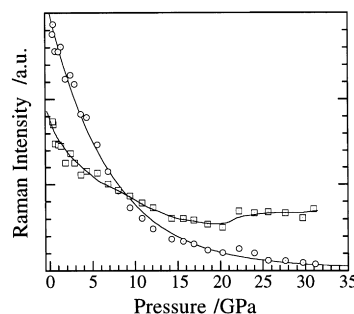


Fig. 2. Integrated intensity of the line at  $260\text{ cm}^{-1}$  ( $\odot$ ) and of the bands comprised between  $602$  and  $650\text{ cm}^{-1}$  ( $\boxtimes$ ) with increasing pressure.

spray-pyrolysis technique [14]. X-ray diffraction diagram is closely similar to that of the tetragonal  $\text{ZrO}_2$  phase with space group  $D_{4h}^{15}$  ( $P4_2/nmc$ ,  $Z = 2$ ). In a cubic set of axes the unit cell is defined by  $c = 5.187\text{ \AA}$ ,  $cla = 1.020$ . The oxygen shift from the ideal fluorite position is given by  $\Delta = 0.045c$ . The crystallite size has been estimated from the half width of the diffraction lines with Scherrer's formula and has been found close to  $18\text{ nm}$  [15].

Raman spectra were obtained using an XY Dilor multi-channel spectrometer equipped with a CCD detector. The  $514.53\text{ nm}$  line from an Argon ion laser was used as the excitation source. Incident powers of about  $10\text{ mW}$  on the sample were used. It has been checked by using  $1$  and  $0.1\text{ mW}$  incident powers that the laser did not induce any thermal effect.

A backscattering geometry was used for illuminating and observing the sample in the diamond anvil cell. An inconel gasket was used as the sample chamber. The pressure-transmitting medium was a 4:1 ethanol–methanol mixture. After focusing with a  $20\times$  magnification microscope objective, the laser spot was about  $2\text{ }\mu\text{m}$  in diameter. R1 and R2 ruby fluorescence lines were used as internal indicators of the applied pressure [16]. Experimental errors were estimated to be  $\pm 0.1\text{ GPa}$ .

All the spectra were decomposed into lorentzian component using Jandel's Peakfit software. The wavenumber accuracy is about  $0.1\text{ cm}^{-1}$  for low-pressure range and about  $5\text{ cm}^{-1}$  above  $20\text{ GPa}$ .

## 3. Results

Raman spectra obtained at room temperature with increasing compressive pressure from atmospheric to  $31\text{ GPa}$  are shown in Fig. 1. In the low-pressure range (i.e. up to  $10\text{ GPa}$ ) the lines of the tetragonal structure shift toward higher frequencies with increasing pressure, except for the  $260\text{ cm}^{-1}$  line which shifts toward lower frequencies. At higher pressure the behaviour of the two low frequency lines show a non-crossing phenomenon. At  $22\text{ GPa}$  the two

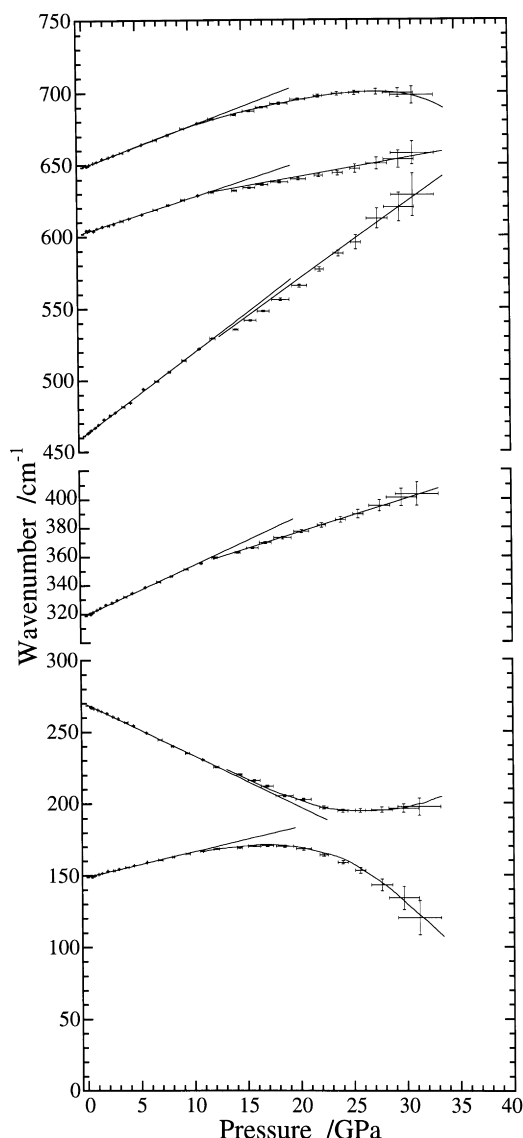


Fig. 3. Pressure dependence of Raman frequency for the bands at 150, 260, 320, 480, 602 and 650  $\text{cm}^{-1}$ . In the low pressure range ( $<10$  GPa) the solid lines correspond to linear regressions. The slopes are given in Table 1.

lines are very close and for higher pressure the line initially at 150  $\text{cm}^{-1}$  changes its behaviour and begins to shift toward lower frequencies. We observe an important broadening of this line and its progressive disappearance in the Rayleigh line.

Notice the global loss of Raman intensity for pressure larger than 24 GPa. The spectrum seems to tend toward a single broad line centred at about 700  $\text{cm}^{-1}$ . We report in Fig. 2 the evolution with increasing pressure of the Raman integrated intensity of the 260  $\text{cm}^{-1}$  line along with that of the bands comprised between 602 and 650  $\text{cm}^{-1}$  line

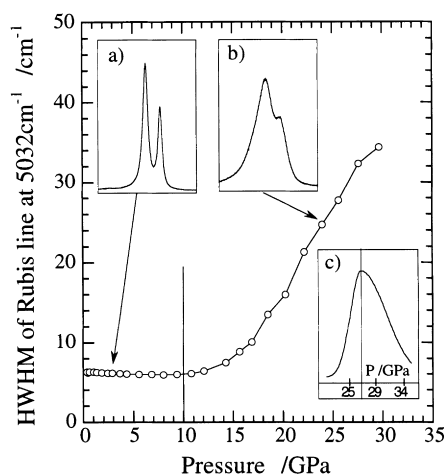


Fig. 4. Pressure dependence of Lorentzian Half Width at Half Maximum (HWHM) of the ruby line at 5032  $\text{cm}^{-1}$ . (a) Ruby spectrum at 3 GPa. (b) Ruby spectrum at 27 GPa. (c) Distribution of pressure around 27 GPa responsible for the broadening of spectrum (b) see Appendix A.

follows a tremendous decrease, while the intensity of the high frequency lines starts to increase again for pressures higher than 20 GPa.

The pressure dependence of the Raman bands frequency is plotted in Fig. 3. This dependence is rather linear for pressure below 10 GPa. The  $(\partial\nu/\partial P)_T$  obtained by linear regression are listed in Table 1. We also report those measured by Cai et al. [17] under uniaxial stress on a polycrystalline  $\text{Y}_2\text{O}_3$  (5.3 wt%) stabilised tetragonal zirconia, as well as those approximately extracted from the Raman spectra obtained by Alzyab et al. [18] under hydrostatic pressure on a polycrystalline  $\text{Y}_2\text{O}_3$  (5 wt%) stabilised tetragonal zirconia. Our results are in good agreement with Alzyab's spectra. The slopes given by Cai et al. cannot be directly compared with ours because they correspond to uniaxial stress applied on the polycrystal. However, their slopes follow the same general trend.

For pressures higher than 12 GPa, we observed a striking slope discontinuity for all the lines. This discontinuity corresponds to the beginning of the repulsion between the two low frequency modes. Notice that by extrapolation, the high frequencies broad feature centred between 560 and 680  $\text{cm}^{-1}$  is expected to merge into a single line centred at 650  $\text{cm}^{-1}$  at high pressures.

The pressure dependence of the Lorentzian Half Width at Half Maximum (HWHM) used in the deconvolution of the ruby R1 line are presented in Fig. 4. For pressure up to 10 GPa the ruby line remains narrow. A typical spectrum taken at 3 GPa is shown in Fig. 4(a). At higher pressures this line broadens because the transmitting medium is no more hydrostatic. The bandshape is asymmetrically broadened by the presence of a pressure gradient. This broadening is shown for the ruby lines at 27 GPa in Fig. 4(b) and the

Table 1

Parameters extracted from linear regressions for pressure lower than 10 GPa. We report those approximately extracted from the Raman spectra obtained by Alzyab et al. [18] under hydrostatic pressure (up to 6.2 GPa) on a polycrystalline  $\text{Y}_2\text{O}_3$  (5 wt%) stabilised tetragonal zirconia as well as those measured by Cai et al. [17] under uniaxial stress on a polycrystalline  $\text{Y}_2\text{O}_3$  (5.3 wt%) stabilised tetragonal zirconia parameters extracted from linear regressions for pressure < 10 GPa

$\nu_0$ ( $\text{cm}^{-1}$ )	$(\partial\nu/\partial P)_T$ ( $\text{cm}^{-1} \text{ GPa}^{-1}$ )	$(\partial\nu/\partial P)_T$ [18] ( $\text{cm}^{-1} \text{ GPa}^{-1}$ )	$(\partial\nu/\partial X)_T$ [17] ( $\text{cm}^{-1} \text{ GPa}^{-1}$ )
149.2	+ 1.75	$\approx$ + 1.6	+ 0.98
269.4	– 3.59	$\approx$ – 3.2	– 0.92
319.4	+ 3.43		+ 1.30
461.6	+ 5.58	$\approx$ + 6.4	+ 2.1
602.5	+ 2.41		Not reported
648.5	+ 2.79	$\approx$ + 3.2	+ 1.1

pressure distribution found to induce this line deformation is presented in Fig. 4(c) (see the explanations in the Appendix A).

The low frequency (150 and  $260 \text{ cm}^{-1}$ ) Raman line's HWHM are shown as a function of pressure in Fig. 5(a). As the pressure increases the HWHMs increase drastically. We report in plain lines the expected HWHM evolution due to the pressure gradient actually measured at each pressure using the broadening of ruby fluorescence spectra. We see that the broadening expected from pressure gradient is not sufficient to reproduce the HWHM of Raman spectra. Notice that such a large broadening is not observed for the other modes as shown in Fig. 5(b) for the mode at  $650 \text{ cm}^{-1}$ . Moreover, at 24 GPa the line at  $260 \text{ cm}^{-1}$  becomes suddenly narrow while the line at  $150 \text{ cm}^{-1}$  becomes very broad. There is an inversion between the HWHM of the two lines. This phenomenon is relevant to the exchange in the intrinsic character of the two modes. This spectral exchange between the two low frequency lines allows the line initially at  $150 \text{ cm}^{-1}$  to continue to shift toward high frequencies and in the same way the line initially at  $260 \text{ cm}^{-1}$  to soften (as shown in Fig. 6). This frequency softening can be represented by a law  $\omega = a(P^c - P)^b$ . The parameters of this law are listed in the legend of Fig. 6. The non-crossover between these two modes is found around  $P_{\text{cr}} = 21 \text{ GPa}$ , and the softening of the  $260 \text{ cm}^{-1}$  mode could drive a structural transition at pressure  $P^0 = 38 \text{ GPa}$ .

#### 4. Symmetry and vibrational selection rules

In the  $\text{ZrO}_2$  tetragonal structure, the six atoms in the primitive cell are localised in the following special positions:  $4d(C_{2v})$  for oxygen (this site corresponds to a tetrahedral site centred on Zr atoms) and  $2a(D_{2d})$  for zirconium. The vibrational Raman active modes are given by:

$$\Gamma = A_{1g} + 2B_{1g} + 3E_g.$$

The eigenvector of the  $A_{1g}$  mode consists in oxygen motions along the  $z$  direction only. The  $B_{1g}$  modes also involve

displacements in the  $z$  direction, however, both zirconium and oxygen are now participating. The  $E_g$  modes consist in displacements of both oxygen and zirconium in the  $(x,y)$  plane [10].

This pronounced polarisation of the collective atomic motions involved in each vibrational mode inclines to use the linear model first introduced by Wieting [19].

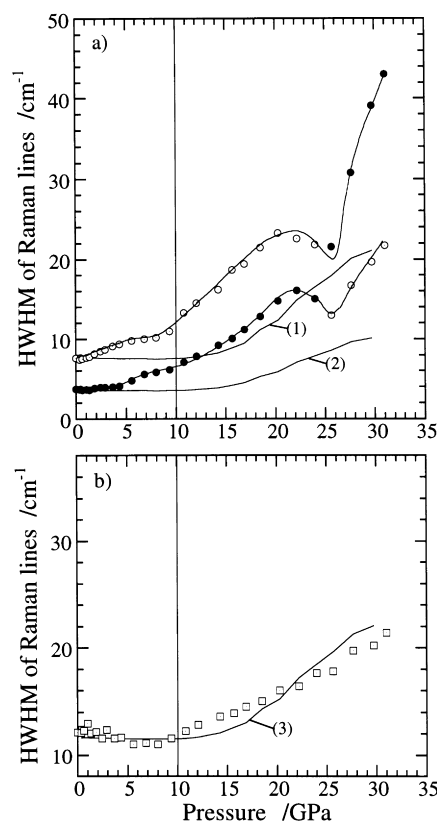


Fig. 5. Pressure dependence of HWHM of low frequency Raman lines: (a) at  $150$  (●) and  $260 \text{ cm}^{-1}$  (○); and (b) at  $650 \text{ cm}^{-1}$ . Curves (1)–(3) correspond to the broadening contribution due to a distribution of pressure in the cell deduced from broadening of ruby line.

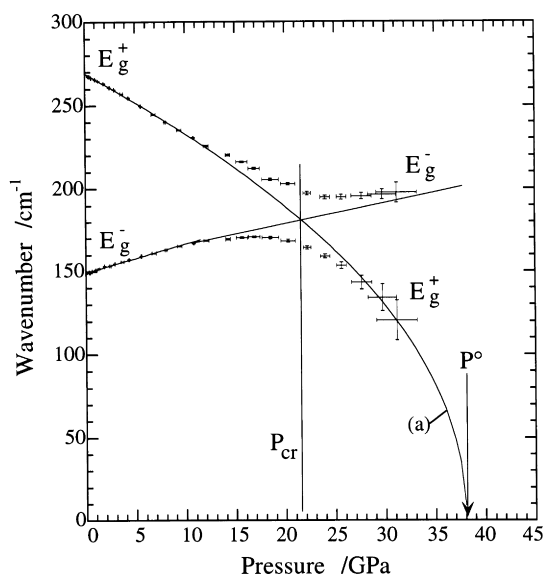


Fig. 6. Pressure dependence of Raman frequency for the bands at 150 ( $E_g^-$ ) and 260  $\text{cm}^{-1}$  ( $E_g^+$ ). The solid line (a) corresponds to  $\omega = a(P^\circ - P)^\frac{1}{2}$  with  $a = 16.25$ ,  $P^\circ = 38.03$  GPa and  $b = 0.472$ . The crossing pressure between the two modes is found around  $P_{cr} = 21$  GPa.

## 5. Discussion

### 5.1. Linear dynamical model

In the linear chain model, the primitive cell is viewed as a succession of six planes perpendicular to the  $z$  direction as depicted in Fig. 7. Each plane contains only one atom of the primitive cell. In a  $k = 0$  normal mode, each plane will move relatively to its neighbours but atoms within a plane are rigidly linked together. The different monoatomic planes in the primitive cell of the  $\text{ZrO}_2$  tetragonal structure are represented by a linear chain of atoms in Fig. 8. To reproduce properties of the tetragonal structure, Mirgorodsky et al underlined the necessity of introducing stretching force constants between zirconium and oxygen and off-diagonal force constant corresponding to angular interaction between zirconium and oxygen [11]. In our linear model, we assume that only the nearest-neighbour planes interact. Consequently, we introduce two different force constants  $C_{d1}$  and  $C_{d2}$  traducing the interaction between zirconium and oxygen planes characterised by two different bond lengths  $\text{Zr}-\text{O}$ . We took the angular interactions into account by introducing a constant  $C_w$  between oxygen  $\text{O}_1-\text{O}_3$  and  $\text{O}_2-\text{O}_4$ . The dynamical equations for the normal vibration of the atomic

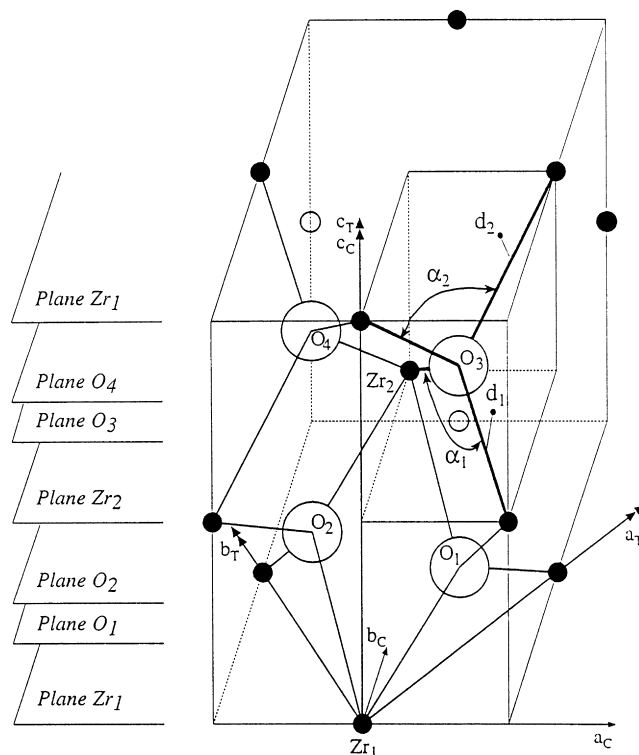


Fig. 7. Primitive cell of tetragonal  $D_{4h}^{15}$  structure [the tetragonal axis ( $a_T, b_T, c_T$ ) are reported as the cubic ones ( $a_C, b_C, c_C$ )]. The different planes of each species are shown at left side of the cell. The tetrahedral oxygen site ( $4d/\text{oxygen O}_3$ ) is located inside the small distorted square in black. The oxygen in the backside of the cell are not represented for better visibility.

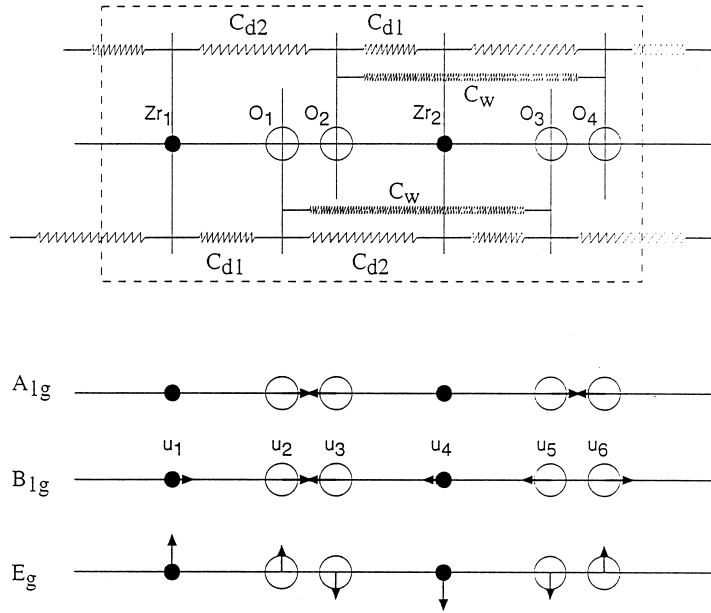


Fig. 8. Schematic representation of the tetragonal cell in the linear chain model. Open circles are oxygen and filled circles are Zirconium. Atomic displacements ( $u_n$ ) associated to each normal mode are represented.

planes can be written as:

$$-M_n \omega^2 u_n = \sum_{m \neq n} C_{nm} (u_m - u_n) \quad (1)$$

where  $M_n$  is the mass of the atom in the  $n$ th plane,  $\omega$  the angular frequency,  $u_n$  and  $u_m$  the normal displacements of the planes  $n$  and  $m$  and  $C_{nm}$  the force constant acting between planes  $n$  and  $m$ .

### 5.2. Determination of eigenvectors

First we will consider the  $A_{1g}$  and  $B_{1g}$  modes.

#### 5.2.1. $A_{1g}$ mode

Consideration of crystal symmetry leads to the following relations between the eigenvector as presented in Fig. 8:  $u_1 = u_4 = 0$  and  $u_2 = -u_3 = u_5 = -u_6$ . Substituting in the six dynamical Eq. (1), a single equation is obtained governing the oxygen motion. The eigenfrequency is given by:

$$\omega_1^2(A_{1g}) = \frac{\alpha}{M_O} \quad (2)$$

where  $\alpha = C_{d1} + C_{d2}$  and  $M_O$  is the oxygen mass ( $15.9994 \text{ g mol}^{-1}$ ), meaning that the frequency of the  $A_{1g}$  mode does not depend upon  $C_w$ .

#### 5.2.2. $B_{1g}$ modes

The plane displacements satisfy the following relationships (Fig. 8):  $u_1 = -u_4$  and  $u_2 = -u_3 = -u_5 = u_6$ . Following the same procedure as above, we obtain a secular equation involving a second-order determinant.

The two eigenfrequencies verify:

$$[M_{Zr} \omega^2(B_{1g}) - 2\alpha][M_O \omega^2(B_{1g}) - (\alpha + 2C_w)] - 2\beta^2 = 0 \quad (3)$$

where  $\alpha = C_{d1} + C_{d2}$ ,  $\beta = C_{d1} - C_{d2}$  and  $M_{Zr}$  is the zirconium mass ( $91.224 \text{ g mol}^{-1}$ ). The sum of the squared solutions  $\omega_2(B_{1g})$  and  $\omega_3(B_{1g})$  of the second order Eq. (3) is given by:

$$[\omega_2^2(B_{1g}) + \omega_3^2(B_{1g})] = \left( \frac{2M_O + M_{Zr}}{M_{Zr}M_O} \right) \alpha + \frac{2C_w}{M_O} \quad (4)$$

The parameter  $C_w$  can be determined by substituting in Eq. (4) the value of  $\alpha$  given by Eq. (2) with experimental frequency  $\omega_1(A_{1g})$ .

$$C_w = \frac{M_O}{2} \left[ (\omega_2^2(B_{1g}) + \omega_3^2(B_{1g})) - \left( \frac{2M_O + M_{Zr}}{M_{Zr}} \right) \omega_1^2(A_{1g}) \right] \quad (5)$$

The parameter  $\beta$  can be extracted from Eq. (3) using  $\alpha$  and  $C_w$  given by Eqs. (2) and (5), respectively.

$$\beta^2 = \frac{M_O M_{Zr}}{2} \left[ \omega_2^2(B_{1g}) - \frac{2M_O}{M_{Zr}} \omega_1^2(A_{1g}) \right] \times \left[ \frac{2M_O}{M_{Zr}} \omega_1^2(A_{1g}) - \omega_3^2(B_{1g}) \right] \quad (6)$$

The experimental frequencies  $\omega_1(A_{1g})$ ,  $\omega_2(B_{1g})$  and  $\omega_3(B_{1g})$  allow the determination of all parameters  $\{\alpha, \beta$  and  $C_w\}$  or  $\{C_{d1}, C_{d2}$  and  $C_w\}$ .

From Eq. (6), it can be noticed that  $\omega_1(A_{1g})$ ,  $\omega_2(B_{1g})$  and  $\omega_3(B_{1g})$  must satisfy at least one of the following conditions.

Otherwise  $\beta^2$  is imaginary and thus  $\beta$  is not defined.

$$\omega_3(\text{B}_{1g}) \leq \left(\frac{2M_O}{M_{Zr}}\right)^{1/2} \omega_1(\text{A}_{1g}) \leq \omega_2(\text{B}_{1g}) \quad (7a)$$

$$\omega_2(\text{B}_{1g}) \leq \left(\frac{2M_O}{M_{Zr}}\right)^{1/2} \omega_1(\text{A}_{1g}) \leq \omega_3(\text{B}_{1g}) \quad (7b)$$

### 5.2.3. $E_g$ modes

We have also undertaken the same calculation for  $E_g$  modes. In order to simplify the mathematical treatment, we assumed that the shearing force constants between planes  $\text{Zr}_1\text{--O}_1$  and planes  $\text{Zr}_1\text{--O}_4$  are equal even if the  $\text{O}_1$  and  $\text{O}_4$  oxygens have slightly different displacement direction inside each plane (notice that the displacement modulus are equal).

The secular equation involves a third order determinant. The three eigenfrequencies are expected to satisfy:

$$\{M_O\omega^2(E_g) - \alpha\} \{[M_{Zr}\omega^2(E_g) - 2\alpha][M_O\omega^2(E_g) - (\alpha + 2C_w)] - 2\beta^2\} = 0 \quad (8)$$

This equation is similar to Eqs. (2) and (3) which were written above for  $\text{A}_{1g}$  and  $\text{B}_{1g}$  modes. However, force constants are now shearing force constants and are written as:

$$\alpha = C_{d1}^s + C_{d2}^s, \quad \beta = C_{d1}^s - C_{d2}^s \quad \text{and} \quad C_w^s.$$

### 5.3. New assignment for $P = 1 \text{ atm}$

Feinberg et al. [13] using polarisation measurements on tetragonal stabilised zirconia proposed the following symmetry assignment:

$$\text{B}_{1g}(155 \text{ cm}^{-1}), \text{E}_g(266 \text{ cm}^{-1}), \text{B}_{1g}(326 \text{ cm}^{-1}), \\ \text{E}_g(474 \text{ cm}^{-1}), \text{A}_{1g}(616 \text{ cm}^{-1}) \text{ and } \text{E}_g(645 \text{ cm}^{-1})$$

These assignments were criticised by Mirgorodsky et al. [12]. They stated that the  $\text{A}_{1g}$  mode, which plays a primary role in the changes of dynamical properties of  $\text{ZrO}_2$  must be at lower frequency to account for the decrease of volume elasticity at the  $c$ – $t$  phase transition.

Eq. (7) cannot be satisfied considering the  $\text{A}_{1g}$  and  $\text{B}_{1g}$  frequencies given by Feinberg et al. [13]. Thus  $\beta$  is not defined and  $C_w = -1.72 \text{ N cm}^{-1}$ . The negative value for  $C_w$  has no physical meaning indicating that Feinberg's assignments have to be reconsidered.

Our model shows that this  $\text{A}_{1g}$  mode is exclusively controlled by  $\text{Zr--O}$  interactions. The oxygen are in a tetrahedral zirconium environment characterised by two types of  $\text{Zr--O}$  bond length: two short bonds ( $d_1 = 2.087$ ) define a  $\text{Zr--O--Zr}$  angle  $2\alpha_1$  with  $\alpha_1 = 59.447^\circ$  and two other long bonds ( $d_2 = 2.362$ ) defining  $\alpha_2 = 49.561^\circ$  (see the small square in Fig. 6). Because of their site symmetry, the zirconium atoms must stay at rest in the  $\text{A}_{1g}$  mode. A small oxygen displacement in the  $z$  direction will create a restoring

force given by  $f = -(2k_1 \cos \alpha_1 + 2k_2 \cos \alpha_2)\Delta z$ . This means that the semi-microscopic force constants introduced in our model can be considered as derived mainly from the projection along the  $z$  direction of  $\text{Zr--O}$  stretching force constant. With these considerations, one can write,  $C_{d1} = 2k_1 \cos \alpha_1$  and  $C_{d2} = 2k_2 \cos \alpha_2$ . Note that the bending force constants are not considered in the  $C_{di}$  projections. However, they are partly taken into account in the  $C_w$  parameter.

In this spirit, we tried to find a triplet of frequencies  $\{\omega_1(\text{A}_{1g}), \omega_2(\text{B}_{1g}) \text{ and } \omega_3(\text{B}_{1g})\}$  that leads to correct values of  $k_1$  and  $k_2$  with regard to the bond force constant-bond length dependence given by Michel et al. [20]. We found that the correct triplet can only be  $\omega_1(\text{A}_{1g}) = 602 \text{ cm}^{-1}$ ,  $\omega_2(\text{B}_{1g}) = 319 \text{ cm}^{-1}$  and  $\omega_3(\text{B}_{1g}) = 648 \text{ cm}^{-1}$ . This leads to  $k_1 = 2.36$ ,  $k_2 = 0.79$  and  $C_w = 0.15 \text{ N cm}^{-1}$  in good agreement with Michel's data.

Under these considerations we propose the following new assignment:

$$\text{E}_g(149 \text{ cm}^{-1}), \text{E}_g(269 \text{ cm}^{-1}), \text{B}_{1g}(319 \text{ cm}^{-1}), \\ \text{E}_g(461 \text{ cm}^{-1}), \text{A}_{1g}(602 \text{ cm}^{-1}) \text{ and } \text{B}_{1g}(648 \text{ cm}^{-1})$$

In this new assignment the  $E_g$  modes appear at rather low frequency. The shear constants values are found equal to  $C_{d1}^s = 0.53$ ,  $C_{d2}^s = 0.16$  and  $C_w^s = 0.65 \text{ N cm}^{-1}$ .

From an elastic point of view, the  $E_g$  modes are related with the  $C_{44}$  component of the elastic tensor [21]. Based on the data given in the literature for  $\text{ZrO}_2$  tetragonal structure [1,12], the shear elastic constant are always at least 25% smaller than the compression elastic constant  $C_{11} \pm C_{12}$  or  $C_{33}$  which are related to  $\text{A}_{1g}$  or  $\text{B}_{1g}$  modes. This gives a justification for the lower values of  $C_{d1}^s$  and  $C_{d2}^s$  found for the  $E_g$  modes. The  $C_w^s$  constant is surprisingly large but its value should be even larger when basing its calculation on previous assignments.

### 5.4. Non-crossover

The above reassignment provides an explanation for the non-crossover behaviour observed for the two  $E_g$  modes at low frequency. Being of the same symmetry, these modes cannot have the same energy. Under increasing pressure, the mode at  $260 \text{ cm}^{-1}$  starts to soften. The pressure evolution of the HWHM shows that the two modes undergo a hybridisation and that they exchange their spectral characteristics when their energies become close to each other.

Furthermore, we see in Fig. 5 that the broadening of  $E_g$  modes at  $150$  and  $260 \text{ cm}^{-1}$  cannot be exclusively described by pressure gradients contribution. Thus, there is another phenomenon, which participate to this additional broadening of Raman lines. This broadening with increasing pressure was first interpreted by Alzyab et al. [18] and Cai et al. [17] as a gradual transformation toward a disordered structure. However, such an additional broadening is not observed for  $\text{A}_{1g}$  and  $\text{B}_{1g}$  modes. Thus we believe that this additional contribution to the HWHM corresponds to strong



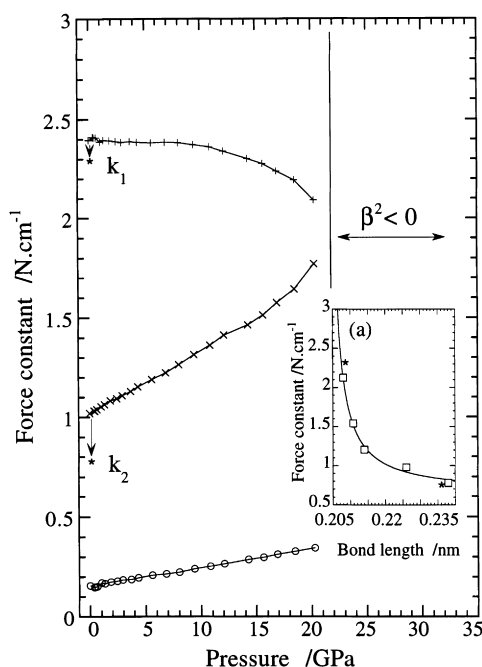


Fig. 9. Pressure dependence of compressional force constant  $C_{d1}$  (+) and  $C_{d1}$  (x) and  $C_w$  (o) extracted from Eqs. (2) and (3) and determined from the pressure dependence of  $B_{1g}(319)$ ,  $A_{1g}(602)$  and  $B_{1g}(648 \text{ cm}^{-1})$  modes. The microscopic force constants  $k_1$  and  $k_2$  (\*) are reported under arrow and compared with Michel et al. [20] data in (a).

damping between these  $E_g$  modes even if their width (corrected from pressure gradients contribution) are slightly smaller than the difference of their frequencies at the non-crossover pressure  $P_{cr}$  (see Figs. 5 and 6).

### 5.5. Pressure dependence of the force constants

The pressure dependence of the force constants introduced in the model are represented in Fig. 9. They are deduced from the pressure dependence of  $B_{1g}(319 \text{ cm}^{-1})$ ,  $A_{1g}(602 \text{ cm}^{-1})$  and  $B_{1g}(648 \text{ cm}^{-1})$  modes using Eqs. (1), (5) and (6). For low pressure the force constant  $C_{d1}$  remains constant whereas  $C_{d2}$  increases with increasing pressure.

At 12 GPa,  $C_{d1}$  starts to decrease and this is associated to the slope discontinuity observed on the frequencies evolutions with pressure. In this pressure range the constant  $C_w$  slowly increases. At 22 GPa, an interesting phenomenon is observed. The adjustment of the wavenumber of  $A_{1g}$  and  $B_{1g}$  modes requires that  $\beta$  tends toward zero and thus that  $C_{d1}$  approaches  $C_{d2}$ . For higher pressures  $\beta^2 < 0$  and thus  $\beta$  cannot be defined as a real. This corresponds to the limit of validity of our model. This means that at these pressures the interactions between zirconium and oxygen planes become equal. Note that the exchange of the low frequencies  $E_g$  modes also takes place at this pressure although these modes do not depend on the same parameters.

This is likely due to a deformation of the tetragonal cell along the  $z$ -axis and to a structural evolution toward the fluorite type structure. The cubic evolution is further confirmed by the decrease of Raman intensity of most of the bands except the high pressure single line centred at  $650 \text{ cm}^{-1}$ , which could correspond to the  $T_{2g}$  mode of a real fluorite structure. In order to compare with the single Raman frequency of fluorite type structure like  $\text{TCeO}_2$  ( $463 \text{ cm}^{-1}$ ),  $\text{ThO}_2$  ( $465 \text{ cm}^{-1}$ ) or  $\text{UO}_2$  ( $467 \text{ cm}^{-1}$ ) [6] it must be corrected from the applied pressure. Applying the pressure dependence of the  $T_{2g}$  phonon frequency given by Cai et al. [22] in cubic stabilised zirconia to the above band at  $650 \text{ cm}^{-1}$  gives for  $P = 1 \text{ atm}$  a frequency close to  $467 \text{ cm}^{-1}$  in agreement with the earlier predictions of Feinberg et al. [13].

Notice that consequently, the broad peak observed for  $P = 1 \text{ atm}$  near  $600 \text{ cm}^{-1}$  in cubic stabilised zirconia would rather correspond to a maximum of density of state rather than to the  $T_{2g}$  Raman active mode. Otherwise the presence of vacancies in the high temperature or stabilised disordered cubic structure would create local stresses giving rise to a distribution of frequency shifts able to generate a high frequency broad asymmetric peak. Equivalent frequency shift can be obtained by a compressive pressure of about 15 GPa.

### 5.6. Soft mode and phase transition

All along the probable continuous deformation towards the high-pressure fluorite-like structure, the  $E_g$  mode at  $260 \text{ cm}^{-1}$  exhibits a soft mode behaviour. The evolution of this mode before and after its hybridisation with the other  $E_g$  mode at  $150 \text{ cm}^{-1}$  is represented by the curve (a) in Fig. 6. This curve can be fitted with a law of the type  $\omega^2 = \alpha(P^\circ - P)^\beta$  where  $P^\circ = 38.03 \text{ GPa}$  and  $\beta = 0.945$  is close to unity. In the Landau theory, a similar law where  $T$  replace  $P$  and  $\beta = 1$  is characteristic of soft modes ferroelectric transitions [23]. The soft mode spectroscopy has given rise to abundant literature. In particular, in second order transition Landau's theory, the soft mode must be totally symmetric in the low symmetry phase. In the present case the soft mode being of  $E_g$  symmetry, the high pressure phase should be of a lower symmetry than tetragonal. Actually, at short range the coordination of zirconium could become less anisotropic and give rise to a distorted fluorite structure. Weak features close to 500 and  $300 \text{ cm}^{-1}$  become visible at high pressure and could be attributed to the presence of the cotunnite phase. Actually these very weak bands become observable because the intensity of the rest of the spectrum decreases (see Fig. 2) but were likely already present at low pressure (hidden under strong bands). These bands do not change in frequency when pressure increases from 10 to 31 GPa and cannot be associated to the sample and in particular to the presence of cotunnite phase. They correspond likely to artefacts (likely scattering from optical elements) and have a too low intensity to merit to be discussed. A

Table 2

Microscopic parameters used in the determination of microscopic compressibility coefficients for the tetragonal structure. The variation with  $P$  of the microscopic force constant is known from Michel data [20]:  $\partial k_i/\partial d_i = -A(d_i - d_0)^{-2}$  with  $A = 16.1 \times 10^{-3} \text{ N cm}^{-1} \text{ nm}$  and  $d_0 = 0.2035 \text{ nm}$ .

The tetragonal parameters  $x, z, \alpha_1, d_1, \alpha_1$  and  $d_2$  are measured from X-ray diffraction diagram at  $P = 1 \text{ atm}$ . The Mathematical expressions extracted from simple geometric considerations are given below:  $\partial d_1/\partial P = -d_1[(2\sqrt{2}x)^{-2} + z^2]^{-1}[(2\sqrt{2}x)^{-2}\chi_1 + z^2\chi_3]$   $\partial d_2/\partial P = -d_2[(2\sqrt{2}x)^{-2} + (1/2 - z)^2]^{-1}[(2\sqrt{2}x)^{-2}\chi_1 + (1/2 - z)^2\chi_3]$   $\partial \alpha_1/\partial P = -(2\sqrt{2}xz)^{-1}[\chi_1 - \chi_3]$   $\partial \alpha_2/\partial P = -(\sqrt{2}x(1/2 - z))^{-1}[\chi_1 - \chi_3]$

$x = 1.020, z = 0.2046$	$\partial C_{di}/\partial P (\text{N cm}^{-1}) \text{ GPa}^{-1}$	$\partial k_i/\partial d_i (\text{N cm}^{-1} \text{ nm}^{-1})$	$\partial d_i/\partial P (\text{nm GPa}^{-1})$	$\partial \alpha_i/\partial P (^\circ \text{ GPa}^{-1})$
$d_1 = 0.2087 \text{ nm}, \alpha_1 = 59.447^\circ$	$-1.837\text{E-}3$	$-253.35$	$-(0.155\chi_1 + 0.054\chi_3)$	$-1.694(\chi_1 - \chi_3)$
$d_2 = 0.2362 \text{ nm}, \alpha_1 = 49.561^\circ$	$3.029\text{E-}2$	$-12.79$	$-(0.137\chi_1 + 0.099\chi_3)$	$-1.173(\chi_1 - \chi_3)$

further exploration of this soft mode using high pressure Raman spectroscopy seems to be difficult because as the frequency drops the line broadens and disappears in the Rayleigh line. Thus it would require to work on a perfect single crystal to limit the Rayleigh diffusion and/or to use another transmitting medium (like He or liquid Nitrogen) to keep a perfect hydrostaticity at higher pressure.

### 5.7. Thermoelastic constants

The Raman spectrum indicates that the structure remains tetragonal for low pressures ( $< 10 \text{ GPa}$ ). With this geometrical constraint it is possible to express the deformation of the tetrahedral unit under isostatic pressure by introducing two different coefficients of compressibility which are defined as  $\chi_1 = -(1/a)(\partial a/\partial P)_T$  along the  $a$  or  $b$  axes and  $\chi_3 = -(1/c)(\partial c/\partial P)_T$  along  $c$ -axis. If we assume that  $\chi_1 P$  and  $\chi_3 P$  remain small in the chosen pressure range, we can express  $d_i = f(x, z, \chi_1, \chi_3, P)$  and  $\alpha_i = g(x, z, \chi_1, \chi_3, P)$  as linear function of  $P$  where  $x = c/a$  and  $z = 1/4 - \Delta$  are the two tetragonal parameters. With increasing pressure, we see that the two force constants  $C_{d1}$  and  $C_{d2}$  exhibit a rather linear pressure dependence. The corresponding derivatives are listed in Table 2. On the contrary, we assumed that these force constants are linked with microscopic ones by a relation of type  $C_{di} = 2k_i \cos \alpha_i$  with  $i = 1, 2$ . Then a derivation for  $P$  allows to express the slope in terms of microscopic parameters:

$$\frac{\partial C_{di}}{\partial P} = 2 \cos(\alpha_i(P)) \frac{\partial k_i(P)}{\partial d_i(P)} \frac{\partial d_i(P)}{\partial P} - 2k_i(P) \sin(\alpha_i(P)) \frac{\partial \alpha_i(P)}{\partial P} \quad (9)$$

This expression is valid for all  $P$  in the chosen range of pressure and a fortiori for  $P = 1 \text{ atm}$ . Then  $\partial k_i/\partial d_i$  is known from Michel et al. data at any  $d_i$ . The values of  $\partial d_i/\partial P$  and  $\partial \alpha_i/\partial P$  are directly linked with the coefficients of compressibility and their expression obtained from simple geometric considerations are listed in Table 2.

The resolution of this equation for  $C_{d1}$  and  $C_{d2}$  allows to extract the microscopic coefficients of compressibility:  $\chi_1 = 5.7 \times 10^{-12}$  and  $\chi_3 = 38.5 \times 10^{-12} \text{ Pa}^{-1}$ . This result means that for isostatic pressure the deformation along  $c$ -axis is seven times larger than along  $a$  or  $b$  axes. The anisotropy

could effectively be at the origin of the structural evolution toward a fluorite type structure. The  $\chi_3$  coefficient is somewhat larger than the usual values. For instance, the application of in expression (11) Ref. [24], within the polyhedral model developed by Hazen, gives a compressibility of  $1.110 \times 10^{-12} \text{ Pa}^{-1}$ . Actually at the difference with our assumption,  $\chi_1$  and  $\chi_3$  may not remain constant in the chosen pressure range. In addition the compound is in a highly anharmonic regime and it could explain its rather large compressibility in this pressure range. High-pressure micro-diffraction experiments are planned in the near future.

## 6. Conclusion

A Raman high-pressure study has been performed on pure nanocrystallised tetragonal zirconia up to  $31 \text{ GPa}$ . The low frequency modes exhibit an over-damped soft mode behaviour that leads us to reconsider the previous normal mode assignment. The reassignment is based on normal mode calculations using a linear chain model. The deduced compressional force constants are in good agreement with force constants reported by Micheal et al and their evolution with increasing pressure is likely associated with a phase transition towards a distorted fluorite-like structure which is confirmed by the continuous evolution of the Raman spectrum towards a single band. In the same respect the microscopic compressibility coefficients estimated from force constants tend to equalize at high pressure.

## Acknowledgements

N. Rosman is acknowledged for his technical assistance on high pressure measurements. We are grateful to E. Djurado who has provided us the sample. E. Anastassakis and T. Pagnier are acknowledged for useful discussions.

## Appendix A

In order to extract a pressure distribution within the cell, we assume that the fluorescence signal measured for each applied pressure is the sum of many elementary signals which are represented by a Lorentzian curve  $L(\omega_k, \Gamma_k, A_k)$

where  $\omega_k$  is the frequency,  $\Gamma_k$  the Half Width at Half Maximum (HWHM) and  $A_k$  the amplitude.

The frequency of each elementary signal is only dependent upon the pressure. The shift of R1 and R2 ruby fluorescence lines with pressure is already well known [16].  $\Gamma_k$  is assumed to remain constant, and  $A_k$  amplitudes correspond to the pressure distribution within the cell which is actually drawn in Fig. 4(c).

The measured signal is the mathematical sum of all these elementary signals.

$$\frac{I(\omega)}{I_0 \zeta_\omega F_{\text{opt}}} = \sum_{k=1}^n \frac{1}{\pi \Gamma_k} \frac{A_k}{1 + \left[ \frac{\omega - \omega_k}{\Gamma_k} \right]^2}$$

where  $I_0$  is the incident irradiance (in  $\text{W cm}^{-2}$ ),  $\zeta_\omega$  the average cross section of the mode at wavenumber  $\omega$  (in  $\text{cm}^2 \text{ molecule}^{-1} \text{ str}^{-1}$ ) and  $F_{\text{opt}}$  is the instrumental function taking into account the real analysed volume, the solid angle of collection and the transmission through the optics.

## References

- [1] G. Teufer, *Acta Cryst.* 15 (1962) 1187.
- [2] C.J. Howard, E. Kisi, O. Ohhtaka, *J. Am. Ceram. Soc.* 74 (1991) 2321.
- [3] L.-G. Liu, *J. Phys. Chem. Solids* 41 (1979) 331.
- [4] J. Haines, J.M. Leger, S. Hull, J.P. Petit, A.S. Pereira, J.A.H. da Jornada, *J. Am. Ceram. Soc.* 80 (7) (1997) 1910.
- [5] J. Godlewski, P. Bouvier, G. Lucazeau, L. Fayette, Zirconium in nuclear chemistry, 12th International Symposium, Toronto, 1998, in press.
- [6] D. Michel, Y. Perez, M. Jorba, R. Collongues, *J. Raman Spectr.* 5 (1976) 163.
- [7] C.H. Perry, D.W. Liu, R.P. Ingel, *J. Am. Ceram. Soc.* 68 (8) (1985) C184.
- [8] S. Lawson, *J. Eur. Ceram. Soc.* 15 (1995) 485.
- [9] K. Negita, *Acta. Metall.* 37 (1) (1989) 313.
- [10] K. Negita, H. Takao, *J. Phys. Chem. Solids* 50 (3) (1989) 325.
- [11] A.P. Mirgorodsky, M.B. Smirnov, P.E. Quintard, T. Merle-Méjean, *Phys. Rev. B* 52 (13) (1995) 9111.
- [12] A.P. Mirgorodsky, M.B. Smirnov, P.E. Quintard, *Phys. Rev. B* 55 (1) (1997) 19.
- [13] A. Feinberg, C.H. Perry, *J. Phys. Chem. Solids* 42 (1981) 513.
- [14] E. Djurado, E. Meunier, *J. Solid State Chem.* 140 (1998).
- [15] E. Djurado, P. Bouvier, G. Lucazeau, submitted for publication.
- [16] G.J. Piermarini, S. Block, J.D. Barnett, R.A. Forman, *J. Appl. Phys.* 46 (1975) 2774.
- [17] J. Cai, Y.S. Raptis, E. Anastassakis, *Appl. Phys. Lett.* 62 (22) (1993) 2781.
- [18] B. Alzyab, C.H. Perry, R.P. Ingel, *J. Am. Ceram. Soc.* 70 (10) (1987) 760.
- [19] T.J. Wieting, *Sol. State Commun.* 12 (1973) 931.
- [20] D. Michel, M.T. VanDenBorre, A. Ennaciri, *Adv. Ceram.* 24 (1988) 555.
- [21] S.K. Chan, *Physica B* 150 (1988) 212.
- [22] J. Cai, C. Raptis, Y.S. Raptis, E. Anastassakis, *Phys. Rev. B* 51 (1) (1995) 201.
- [23] C. Kittel, *Introduction to Solid State Physics*, Wiley, New York, 1976.
- [24] R.M. Hazen, in: S.W. Kiefer, A. Navrotsky (Eds.), *Reviews in Mineralogy*, 14, 1985, pp. 324.